The Astrophysical Journal, 975:24 (14pp), 2024 November 1 https://doi.org/10.3847/1538-4357/ad77d1

An X-Ray Significantly Variable, Luminous, Type 2 Quasar at $z = 2.99$ with a Massive Host Galaxy

Xiurui Zhao[1,2], Stefano Marchesi[3,4,5], Marco Ajello[4], Francesca Civano[6], Roberto Gilli[5], Giorgio Lanzuisi[5], Iván E. López[5], Peter G. Boorman[7], Ross Silver[6], Nuria Torres-Albà[4], and Andrealuna Pizzetti[4]
[1] Department of Astronomy, University of Illinois at Urbana-Champaign, Urbana, IL 61801, USA
[2] Center for Astrophysics | Harvard & Smithsonian, 60 Garden Street, Cambridge, MA 02138, USA
[3] Dipartimento di Fisica e Astronomia (DIFA), Università di Bologna, via Gobetti 93/2, I-40129 Bologna, Italy
[4] Department of Physics and Astronomy, Clemson University, Kinard Lab of Physics, Clemson, SC 29634, USA
[5] INAF, Osservatorio di Astrofisica e Scienza dello Spazio di Bologna, via P. Gobetti 93/3, 40129 Bologna, Italy
[6] NASA Goddard Space Flight Center, Greenbelt, MD 20771, USA
[7] Cahill Center for Astrophysics, California Institute of Technology, 1216 East California Boulevard, Pasadena, CA 91125, USA
Received 2024 May 22; revised 2024 August 3; accepted 2024 September 3; published 2024 October 23

Abstract

We present a comprehensive X-ray analysis and spectral energy distribution (SED) fitting of WISEA J171419.96+602724.6, an extremely luminous type 2 quasar at $z = 2.99$. The source was suggested as a candidate Compton-thick (column density $N_{\rm H} > 1.5\times10^{24}\,{\rm cm}^{-2}$) quasar by a short XMM-Newton observation in 2011. We recently observed the source with deep NuSTAR and XMM-Newton exposures in 2021 and found that the source has a lower obscuration of $N_{\rm H} \sim 5\times10^{22}\,{\rm cm}^{-2}$ with an about four times lower flux. The two epochs of observations suggested that the source was significantly variable in X-ray obscuration, flux, and intrinsic luminosity at 2σ–3σ in less than 2.5 yr (in the source rest frame). We performed SED fitting of this source using Code Investigating GALaxy Emission thanks to its great availability of multiwavelength data (from hard X-rays to radio). The source is very luminous, with a bolometric luminosity of $L_{\rm BOL} \sim 2.5 \times 10^{47}\,{\rm erg\,s}^{-1}$. Its host galaxy has a huge star formation rate (SFR) of $\sim$1280 $M_\odot\,{\rm yr}^{-1}$ and a huge stellar mass of $\sim 1.1 \times 10^{12}\,M_\odot$. The correlation between the SFR and stellar mass of this source is consistent with what was measured in the high-z quasars. It is also consistent with what was measured in the main-sequence star-forming galaxies, suggesting that the presence of the active nucleus in our target does not enhance or suppress the SFR of its host galaxy. The source is an infrared hyperluminous, obscured galaxy with a significant amount of hot dust in its torus and shares many similar properties with hot, dust-obscured galaxies.

Unified Astronomy Thesaurus concepts: Active galactic nuclei (16); AGN host galaxies (2017)

1. Introduction

It is widely believed that the powerful emission of active galactic nuclei (AGN) originates from mass accreting onto the central supermassive black hole (SMBH; E. E. Salpeter 1964). Thus, AGN activity can be used as a tracer of SMBH growth. These black holes (BHs) are found to have a mass ranging from 10^6 to $10^{10}\,M_\odot$ (D. J. Mortlock et al. 2011). The large amount of material needed for quick BH growth, particularly near the peak of BH accretion history $z \sim 1.5$–3, is expected to obscure the nuclear emission, implying that SMBH growth may be obscured (N. Menci et al. 2008; A. Merloni & S. Heinz 2008; I. Delvecchio et al. 2014).

Simulations of cosmic X-ray background show that the majority of quickly growing SMBHs in this redshift range are obscured by material with gas column density $\geqslant 10^{23}\,{\rm cm}^{-2}$, and ~40% of them are obscured by Compton-thick (CT; $N_{\rm H} \geqslant 10^{24}\,{\rm cm}^{-2}$) gas (R. Gilli et al. 2007; J. Buchner et al. 2015). This rapid BH growth phase, although extremely important for the BH cosmic accretion history, is mostly inaccessible owing to the lack of detections of luminous, high-z, obscured AGN. Selection techniques based on mid-IR emission have been developed to select candidate CT AGN up to $z = 2$–3 (e.g., E. Daddi et al. 2007). However, the measured obscuring column densities are largely uncertain owing to the lack of (high signal-to-noise ratio (S/N)) X-ray spectra. Currently, most of the X-ray-selected AGN at high z are less obscured, given the bias against detecting obscured (and thus fainter) AGN. Indeed, only a handful of CT AGN (candidates) have been observed in X-rays at $z \gtrsim 1.5$ (e.g., R. Gilli et al. 2011; G. Lanzuisi et al. 2018; B. Snios et al. 2020; F. Vito et al. 2020).

WISEA J171419.96+602724.6 (hereafter J1714+6027) is a type 2 quasar[8] at $z = 2.99$. It was selected from the 4XMM-DR10 catalog (4XMM J171419.3+602721; N. A. Webb et al. 2020) as a CT quasar candidate. The catalog reports that the source has a hardness ratio (HR) of HR $= 0.90^{+0.10}_{-0.16}$, suggesting that J1714+6027 is a heavily obscured quasar. HR is defined as (H − S)/(H + S), where H and S are hard (2–4.5 keV) and soft (1–2 keV) fluxes, respectively. The source was observed with the XMM-Newton MOS2 camera in 2011 March (ObsID: 0651370901), at an off-axis angle of 14.′8. The exposure of the observation is 11.6 ks, but the vignetting-corrected exposure at the source position is only 2.6 ks, resulting in a total number of 12 net counts. We fitted the source spectrum with a simplified phenomenological model (see more details in Section 2.2.1) assuming a photon index of $\Gamma = 1.80$ (a typical value for type 2 AGN; e.g., C. Ricci et al. 2017b). The best-fit "line-of-sight"

[8] Here we define a quasar as an AGN with intrinsic 2–10 keV luminosity $L_{2-10} \geqslant 10^{44}\,{\rm erg\,s}^{-1}$.

Table 1
Summary of NuSTAR and XMM-Newton Observations

Instrument	Sequence ObsID	Start Time (UTC)	End Time (UTC)	Exposure (ks)	Net Count Rate[a] (10^{-3} counts s^{-1})
NuSTAR	60701056002	2021-09-27 T22:36:09	2021-09-30 T05:11:09	108/107	0.82/0.73
XMM-Newton	0890450101	2021-09-28 T06:05:55	2021-09-28 T23:51:51	30/36/17[b]	1.93/2.42/8.11

Notes.
[a] The reported NuSTAR count rates are those of the FPMA and FPMB modules in the 3–16 keV range, respectively. The reported XMM-Newton count rates are those of the MOS1, MOS2, and pn modules in the 0.5–10 keV range, respectively.
[b] The reported XMM-Newton exposures are the cleaned exposure times for MOS1, MOS2, and pn after removing the high-background intervals. The on-source exposure is originally 68 ks.

column density is $N_{\rm H,Z} = 1.1^{+1.9}_{-0.6} \times 10^{24}\,{\rm cm}^{-2}$, suggesting that the source is a CT quasar candidate. The source flux is $\sim 1.6 \times 10^{-13}\,{\rm erg\,s}^{-1}$ in the 2–10 keV band, implying that the source is bright enough for deep X-ray observation follow-up. Therefore, we proposed the source to NuSTAR and XMM-Newton to confirm its CT nature.

The paper is structured as follows: In Section 2, we present the data reduction and spectra analysis of the new X-ray data of the source. In Section 3, we present the multiwavelength data of the source and perform the spectral energy distribution (SED) fitting. In Section 4, we discuss the X-ray and multiwavelength properties (including its variability properties) of the AGN and the properties of its host galaxy.

Uncertainties are quoted at the 90% confidence level throughout the paper unless otherwise stated. The magnitudes used here are in the AB system. Standard cosmological parameters are adopted as follows: $H_0 = 70\,{\rm km\,s}^{-1}\,{\rm Mpc}^{-1}$, $\Omega_M = 0.30$, and $\Omega_\Lambda = 0.70$.

2. X-Ray Data Analysis

J1714+6027 was observed in NuSTAR cycle 7 (PI: Zhao, ID: 7250) on 2021 September 27 with 108 ks NuSTAR and 68 ks XMM-Newton exposures. The details of the observations can be found in Table 1. We reduce the NuSTAR and XMM-Newton data in Section 2.1 and analyze the spectra in Section 2.2. We also reanalyze the 2011 XMM-Newton observation.

2.1. Data Reduction

Both NuSTAR and XMM-Newton observations were reduced using the most updated version of calibration files and software as detailed in the following sections.

2.1.1. NuSTAR

The NuSTAR data were processed using HEASoft v.6.32.1 and NuSTAR Data Analysis Software (NuSTARDAS) v.2.1.2 with the updated calibration and response files CALDB v.20231017. The level 1 raw data were calibrated, cleaned, and screened by running the `nupipeline` tool. As the background event rates are slightly elevated around the SAA, we used the parameters `saamode=OPTIMIZED` and `tentacle=yes` when reducing the data. The source spectra ancillary response files and response matrix files are obtained using the `nuproducts` script. The source spectra are extracted from a 40″ circular region, corresponding to an encircled energy fraction (EEF) of 60% at 10 keV. The spectral extraction radius was determined following the method in L. Zappacosta et al. (2018a) that maximizes both the S/N and the number of net counts. We note that the two X-ray sources WISEA J171430.62+602722.7 (hereafter J171430+602722) and WISEA J171430.09+602635.7 (hereafter J171430+602635) are about 80″ and 90″ from J1714+6027, respectively. They are 54% and 70% fainter than J1714+6027 in the 2–10 keV band, respectively. We also notice another X-ray source, WISEA J171425.30+602928.1 (hereafter J171425+602928), that is about 125″ from J1714+6027 but is 180% brighter than J1714+6027 (in the 2–10 keV band). The selected source spectra extraction region thus includes ∼3% of the fluxes from the first two sources and includes about 0.8% of the flux from the third source in the 2–10 keV band. The details of the spectral analysis and source properties of the three sources are described in Appendix A. Therefore, a limited fraction of about 4.5% of the J1714+6027 flux measured by NuSTAR in the 2–10 keV band is likely to originate from the other three nearby sources. At 10–16 keV, the contaminating flux is about 2.8% based on the best-fit models of the three nearby sources and J1714+6027.

As the number of counts from the background is comparable to those from the source and the NuSTAR background is highly spatially uneven across the field of view (FOV), we analyzed the NuSTAR background using the `nuskybgd` tool[9] (D. R. Wik et al. 2014). This tool provides more accurate modeling of the NuSTAR background, and it has been widely used in the studies of extended or faint targets and extragalactic surveys. We followed the standard method when applying `nuskybgd` to our data (see, e.g., D. R. Wik et al. 2014; X. Zhao et al. 2021a). The accuracy of the simulated background was tested using the same method as in X. Zhao et al. (2021a) before it was used in the spectral analysis. We note that the source flux measured in NuSTAR is consistent with that measured in XMM-Newton (see Section 2.2), indicating that the NuSTAR background is well simulated. Both FPMA and FPMB spectra are dominated by the background at >16 keV; therefore, we only analyzed the NuSTAR data between 3 and 16 keV.

2.1.2. XMM-Newton

The XMM-Newton observation was taken quasi-simultaneously to the NuSTAR one with the EPIC CCD cameras (pn; L. Strüder et al. 2001) and two MOS cameras (M. J. L. Turner et al. 2001): the XMM-Newton observation started at the same time but ended ∼9 hr before the NuSTAR one. We reduced the XMM-Newton data using the Science Analysis System (F. Jansen et al. 2001) version 16.1.0. The light curves of the three cameras are produced using the `evselect` tool at

[9] https://github.com/NuSTAR/nuskybgd

Table 2
Best-fit Results of the 2011 XMM-Newton Spectrum and 2021 NuSTAR+XMM-Newton Spectra with Different Models

Year	Phenome 2011	Phenome 2011	Phenome 2021	MYT_{90} 2021	MYT_0 2021	Borus 2021
C/dof	10/7	10/7	41/52	41/52	40/52	40/52
Γ[a]	1.80^{fix}	1.45^{fix}	$1.45^{+0.19}_{-0.18}$	$1.54^{+0.20}_{-u}$	$1.55^{+0.19}_{-u}$	$1.50^{+0.18}_{-u}$
θ_{obs}[b]	...	...	...	90^{fix}	0^{fix}	60^{fix}
A_S	...	...	...	1^{fix}	1^{fix}	...
$N_{H,Z}$[c]	114^{+188}_{-64}	95^{+172}_{-59}	$5.9^{+4.5}_{-3.6}$	$6.3^{+4.6}_{-3.7}$	$5.8^{+4.4}_{-3.6}$	$5.6^{+4.5}_{-3.1}$
$N_{H,S}$[d]	...	...	...	1.4^{fix}	1.4^{fix}	1.4^{fix}
c_f[e]	...	...	...	...	...	0.20^{fix}
$F_{0.5-2}$[f]	$0.5^{+0.7}_{-0.5}$	$0.5^{+0.7}_{-0.5}$	$1.1^{+0.1}_{-0.1}$	$1.1^{+0.2}_{-0.2}$	$1.1^{+0.2}_{-0.1}$	$1.1^{+0.2}_{-0.1}$
F_{2-10}[g]	16^{+13}_{-9}	17^{+15}_{-9}	$4.6^{+0.6}_{-0.6}$	$4.6^{+0.5}_{-0.6}$	$4.6^{+0.6}_{-0.6}$	$4.6^{+0.6}_{-0.6}$
L_{2-10}[h]	14^{+16}_{-8}	9^{+9}_{-5}	$1.8^{+0.5}_{-0.5}$	$1.8^{+0.7}_{-0.4}$	$1.7^{+0.6}_{-0.5}$	$1.7^{+0.7}_{-0.3}$
L_{10-40}[i]	16^{+19}_{-10}	17^{+18}_{-10}	$3.5^{+0.5}_{-0.6}$	$3.2^{+0.5}_{-0.5}$	$2.9^{+0.5}_{-0.4}$	$3.1^{+0.5}_{-0.4}$

Notes.
[a] The photon index (Γ) of the `MYTorus` and `borus` models is only allowed to vary between 1.4 and 2.6. u means that the 90% confidence lower limit of the photon index is not measured at $\Gamma \geqslant 1.4$.
[b] Angle between the torus axis and the "line-of-sight" direction in degree, e.g., $\theta_{obs} = 90°$ is edge-on and $\theta_{obs} = 0°$ is face-on.
[c] "Line-of-sight" column density in 10^{22} cm^{-2}.
[d] "Global average" column density of the torus in 10^{24} cm^{-2}.
[e] Covering factor of the torus.
[f] 0.5–2 keV flux in 10^{-14} erg cm^{-2} s^{-1}.
[g] 2–10 keV flux in 10^{-14} erg cm^{-2} s^{-1}.
[h] 2–10 keV intrinsic luminosity in 10^{45} erg s^{-1}. The luminosity is derived using "clum" in `xspec`.
[i] 10–40 keV intrinsic luminosity in 10^{45} erg s^{-1}.

>10 keV with `PATTERN==0` (where the events are dominated by the backgrounds rather than the sources in the FOV). Due to the strong background flares (which might be associated with a C-level solar flare[10] during the XMM-Newton observation), 47%–75% of the XMM-Newton exposure was lost, where we removed the time interval with count rates in the FOV larger than 0.15, 0.20, and 0.40 counts s^{-1} in MOS1, MOS2, and pn, respectively. Therefore, the effective exposures used for spectral analysis of the three cameras are 30, 36, and 17 ks, respectively. The source spectra are extracted from a 15″ circular region, corresponding to ≈70% of the EEF at 1.5 keV, while the background spectra are obtained from a 40″ circle located near the source. We visually inspected the XMM-Newton image to avoid contamination to the background from sources near J1714+6027.

We analyzed the XMM-Newton spectra between 0.5 and 10 keV in all three cameras. The net count rates of the two modules of NuSTAR and three cameras of XMM-Newton are reported in Table 1. The NuSTAR and XMM-Newton spectra are grouped with a minimum of 30 and 10 counts per bin using `grppha`, respectively.

2.2. Spectral Analysis

We performed a broadband (0.5–16 keV) spectral analysis of J1714+6027 using `XSPEC` (K. A. Arnaud 1996) version 12.13.1. The photoelectric cross section is from D. A. Verner et al. (1996); the element abundance is from E. Anders & N. Grevesse (1989), and metal abundance is fixed to solar; and the Galactic absorption column density is fixed at 2.2×10^{20} cm^{-2} (`nh` task; HI4PI Collaboration et al. 2016). The C-statistic (W. Cash 1979) is adopted when fitting the spectra. The source redshift is fixed at $z = 2.99$ (M. Lacy et al. 2007).

[10] https://www.swpc.noaa.gov/products/goes-x-ray-flux

We first analyzed the spectra using a simplified phenomenological model considering only the absorption along the line of sight. As the spectra of the heavily obscured AGN were not found to be well described by a simple line-of-sight component, especially at the Compton hump at 10–30 keV (e.g., A. P. Lightman & T. R. White 1988; P. Magdziarz & A. A. Zdziarski 1995; T. Yaqoob 2012), we then fit the spectra of J1714+6027 using two physically motivated models, `MYTorus` (K. D. Murphy & T. Yaqoob 2009) and `borus` (M. Balokovic et al. 2018), including also the reflection from the absorber, which was widely used to model the spectra of heavily obscured AGN with high-quality data (e.g., S. Puccetti et al. 2014; A. Annuar et al. 2015; F. Ursini et al. 2018; S. Marchesi et al. 2018; N. Torres-Albà et al. 2021). The best-fit results are reported in Table 2.

2.2.1. Simplified Phenomenological Model

We first fit the source spectra with a simplified phenomenological absorbed power-law model as described in Equation (1). Here `constant` models the cross-calibration between NuSTAR and XMM-Newton, noted as $C_{NuS/XMM}$; `phabs` models the Galactic absorption; `zphabs` models the quasar intrinsic absorption along the line of sight caused by the obscuring gas and dust surrounding the accreting SMBH; and `zpowerlw` models the quasar intrinsic X-ray emission produced by the hot corona. The phenomenological model (Model A), in `XSPEC` terminology, is thus

$$\text{Model A} = \text{constant} * \text{phabs} * (\text{zphabs} * \text{zpowerlw}). \quad (1)$$

We first leave the $C_{NuS/XMM}$ free to vary when fitting the spectra, which allows us to check the background simulation of NuSTAR. The best-fit cross-calibration is $C_{NuS/XMM} = 1.08^{+0.49}_{-0.20}$, which is consistent with the cross-calibration between NuSTAR and XMM-Newton determined by the International Astronomical Consortium for High Energy Calibration (IACHEC; K. K. Madsen

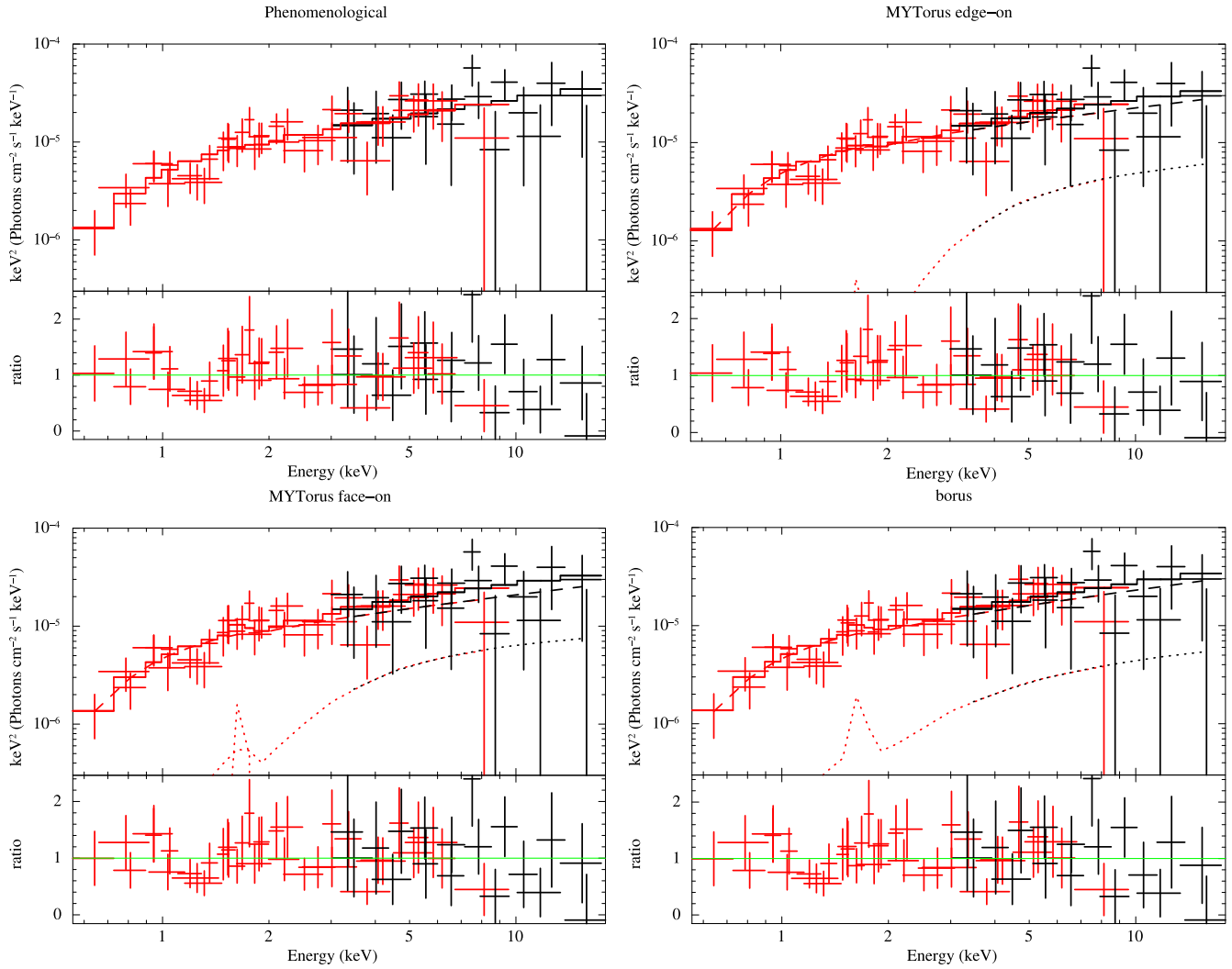

Figure 1. X-ray spectra (in the observed frame) of J1714+6027 fitted using phenomenological, `MYTorus` (edge-on and face-on), and `borus` models. The black and red points correspond to NuSTAR and XMM-Newton data, respectively. The solid, dashed, and dotted lines correspond to the model predictions from the total, line-of-sight component, and reflection components, respectively.

et al. 2017). Due to the limited number of photons, we fixed $C_{\rm NuS/XMM}$ at unity when fitting the spectra to better constrain the other source properties. The best-fit photon index is $\Gamma = 1.45^{+0.19}_{-0.18}$, which is harder than the typical photon indices of an obscured quasar with $\Gamma \sim 1.80$ (e.g., C. Ricci et al. 2017b). The best-fit line-of-sight obscuration is $N_{\rm H,Z} = 5.9^{+4.5}_{-3.6} \times 10^{22}\,{\rm cm}^{-2}$, suggesting that the source is an obscured Compton-thin ($10^{22}\,{\rm cm}^{-2} < N_{\rm H} < 10^{24}\,{\rm cm}^{-2}$) quasar. The best-fit results of the phenomenological model are listed in Table 2, and the source spectra with best-fit models are plotted in Figure 1. We notice that the overall spectral shape is well fitted. The C-statistics divided by degrees of freedom (dof) is $C/{\rm dof} = 41/52$.

2.2.2. Physical Model: `MYTorus`

We then fit the spectra with a physically motivated model `MYTorus` (K. D. Murphy & T. Yaqoob 2009), which models both the line-of-sight continuum of the quasar and the intrinsic emission reflected from the torus. The basic geometry of the `MYTorus` model consists of a torus that has a fixed half-opening angle $\theta_{\rm oa} = 60°$ or a fixed covering factor of $f_c = 0.5$, with a circular cross section. The line-of-sight continuum is modeled by the absorption (`MYTZ`) on a power law. The reflection component is modeled by a Compton-scattered continuum (`MYTS`) and the most prominent fluorescent emission lines (`MYTL`), i.e., the Fe Kα and Fe Kβ lines, at 6.4 and 7.06 keV, respectively. It is worth noting that if the geometry of the torus differs significantly from this one, or if there is a nonnegligible time delay between the intrinsic continuum emission and the Compton-scattered continuum one, i.e., the central region is not compact and the intrinsic emission varies rapidly, the scattered component normalization can significantly differ from the main component one. To take these effects into account, the scattered continuum and the emission-line component are multiplied by a constant, which we define here as A_S.

The configurations of `MYTorus` are very flexible. We used the "decoupled" configuration of `MYTorus` as introduced in T. Yaqoob (2012), assuming that the line-of-sight continuum and the reflection component can in principle have different inclination angles ($\theta_{\rm obs}$, the angle between the torus axis and the line of sight) and column density values. In the "decoupled" configuration, the line-of-sight absorption (`MYTZ`) is modeled with $\theta_{\rm obs,Z} = 90°$, so that the derived $N_{\rm H,Z}$ is the line-of-sight column density rather than the column density along the

equator (see, e.g., X. Zhao et al. 2019, for more details). The inclination of J1714+6027 can be between 0° and 90°, which can be modeled by using two sets of reflection components and using two different A_S. Here we fit the spectra assuming an "edge-on" scenario ($\theta_{\rm obs,S} = 90°$) and a "face-on" scenario ($\theta_{\rm obs,S} = 0°$). However, we note that a much better spectral quality is needed to achieve meaningful constraints on the source properties.

In XSPEC the MYTorus model is described as follows:

$$\text{Model B} = \text{constant} * \text{phabs} * (\text{MYTZ} * \text{zpowerlw} + A_S * \text{MYTS} + A_S * \text{MYTL}). \quad (2)$$

For the "edge-on" scenario, the best-fit photon index is $\Gamma = 1.54^{+0.20}_{-u}$ (MYTorus and borus allow the photon index to vary between 1.4 and 2.6). The best-fit line-of-sight column density is $N_{\rm H,Z} = 6.3^{+4.6}_{-3.7} \times 10^{22}\,{\rm cm}^{-2}$. The torus column density $N_{\rm H,S}$ and A_S are entirely unconstrained. Therefore, we fixed A_S at $A_S = 1$ and fixed $N_{\rm H,S}$ at the average torus column density $N_{\rm H,S,Zhao2021} \sim 1.4 \times 10^{24}\,{\rm cm}^{-2}$ derived from a sample of ∼100 low–redshift Compton-thin AGN (X. Zhao et al. 2021b).

For the "face-on" scenario, the best-fit photon index is $\Gamma = 1.55^{+0.19}_{-u}$. The best-fit line-of-sight column density is $N_{\rm H,Z} = 5.8^{+4.4}_{-3.6} \times 10^{22}\,{\rm cm}^{-2}$. We fixed A_S at $A_S = 1$ and fixed $N_{\rm H,S}$ at $N_{\rm H,S} = 1.4 \times 10^{24}\,{\rm cm}^{-2}$ because they are entirely unconstrained, as well.

2.2.3. Physical Model: Borus

We now fit the spectra using borus (M. Balokovic et al. 2018), another physically motivated model, which can be used to compare the results with those obtained from the MYTorus model. borus assumes the geometry of the torus as a sphere with conical cutouts at both poles, so it allows for variable covering factors. The borus model is composed of a reprocessed component that is reflected by a toroidal structure from the intrinsic emission. Besides the reflection component, we added a "line-of-sight" component modeled by an absorbed cutoff power law. In XSPEC, the borus model is described as

$$\text{Model C} = \text{constant} * \text{phabs} * (\text{borus} + \text{zphabs} * \text{cabs} * \text{cutoffpl}), \quad (3)$$

where zphabs*cabs models the absorption along the "line of sight," which includes the effect of Compton scattering. The cutoff energy $E_{\rm cut}$ of the power law was found to be unconstrained owing to the low quality of the data, so we fix $E_{\rm cut}$ at 150 keV as found in sources with similar luminosities (G. Lanzuisi et al. 2019) to reduce the degeneracy. The best-fit photon index is $\Gamma = 1.50^{+0.18}_{-u}$. The best-fit line-of-sight column density is $N_{\rm H,Z} = 5.6^{+4.5}_{-3.1} \times 10^{22}\,{\rm cm}^{-2}$. The best-fit inclination (the angle between the line of sight and the torus axis) favors a face-on scenario but is not constrained ($\theta = 18^{+55}_{-u}$ deg at 1σ confidence level). To reduce the degeneracy, we fixed the inclination angle at $\theta = 60°$ as suggested in X. Zhao et al. (2020). The torus column density and torus covering factor are both unconstrained. Therefore, we fixed the torus column density at $N_{\rm H,S} = 1.4 \times 10^{24}\,{\rm cm}^{-2}$. We fixed the torus covering factor at $c_f = 0.2$, which was measured in sources with X-ray luminosity similar to that of J1714+6024 (S. Marchesi et al. 2019). This small covering factor is also supported by the SED fitting results in Section 3.2. We note that using a larger covering factor does not alter the best-fit values of other physical properties significantly.

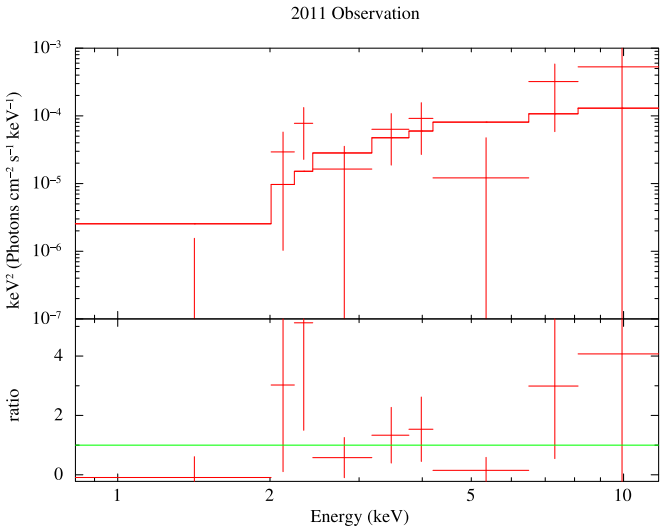

Figure 2. The 2011 XMM-Newton observed X-ray spectrum (in observed frame) of J1714+6027 fitted using the phenomenological model described in Section 2.2.1. The spectra are grouped with a minimum of 2 counts per bin. The red points correspond to the data, and the solid line is the best-fit model prediction.

Both the phenomenological model and physically motivated models, i.e., MYTorus and borus, can well fit the source spectral shape. The best-fit results of the fluxes, line-of-sight column densities, and photon indices of all models are consistent with each other within uncertainties. All models suggest that J1714+6027 is a Compton-thin quasar even after considering the uncertainties. The residuals of both the phenomenological model and the physical model are consistent with each other, suggesting that the source does not present a significant reflection contribution from the torus.

We note that future hard X-ray telescopes, e.g., HEX-P,[11] could provide better characterization of the reflection component of the obscured quasars thanks to their much better sensitivities and photon-collecting capabilities at hard X-rays (P. G. Boorman et al. 2024), thus better constraining the torus properties of quasars like J1714+6027.

2.3. Reanalysis of the 2011 XMM-Newton Observation

As a consistency check, we refit the 2011 XMM-Newton observation that led to a CT estimate of the source line-of-sight column density, this time using the photon index derived from the phenomenological model in the recent deeper observations ($\Gamma = 1.45$). The spectrum and the best-fit model are plotted in Figure 2. The best-fit "line-of-sight" column density is $N_{\rm H,Z} = 9.5^{+17.2}_{-5.9} \times 10^{23}\,{\rm cm}^{-2}$. The best-fit flux of the source in the 2011 observation is $F_{0.5-2} < 1.2 \times 10^{-14}\,{\rm erg\,cm^{-2}\,s^{-1}}$ and $F_{2-10} = 1.7^{+1.5}_{-0.9} \times 10^{-13}\,{\rm erg\,cm^{-2}\,s^{-1}}$. We compare the source spectra of the 2011 observation and the 2021 observations in Figure 3. We plot the contour of the 2–10 keV flux as a function of the line-of-sight column density of the 2011 and 2021 observations in Figure 4. The best-fit intrinsic luminosity of the source in the 2011 observation is $L_{2-10} \sim 9 \times 10^{45}\,{\rm erg\,s^{-1}}$, which is about 5 times more luminous than what was measured in 2021.

[11] https://hexp.org

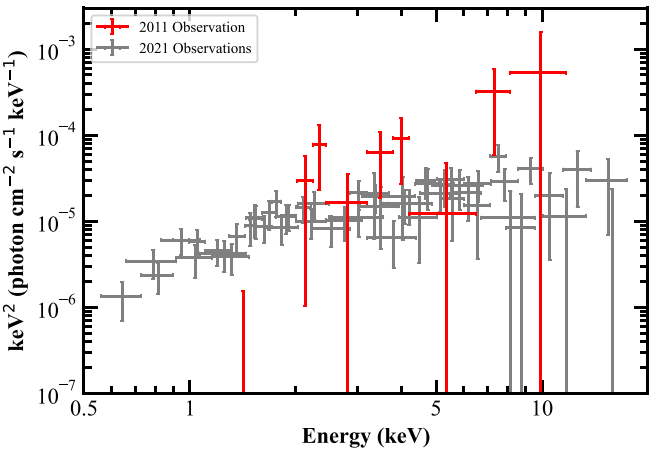

Figure 3. Unfolded spectra of the XMM-Newton observation in 2011 (red) and XMM-Newton + NuSTAR observations in 2021 (gray). Both the 2011 and 2021 spectra are modeled using the phenomenological model. The 2011 observation is modeled assuming a photon index of 1.45.

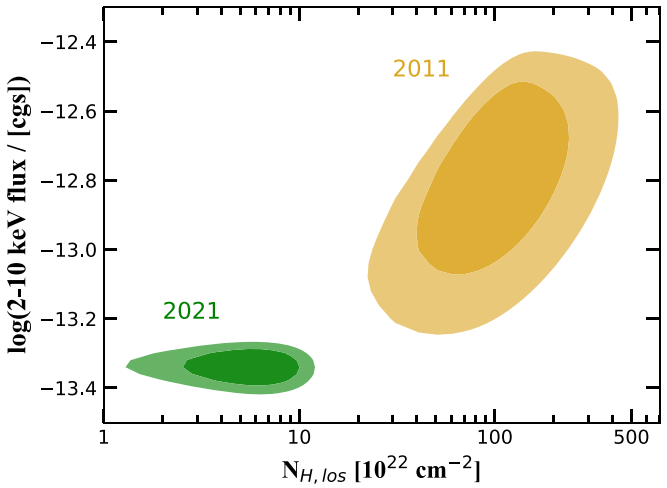

Figure 4. Contour of the 2–10 keV flux as a function of the line-of-sight column density of the 2011 (yellow) and 2021 (green) observations. We present the fitting results from the phenomenological model of both observations. The dark and light colors represent the 68% and 90% confidence levels, respectively.

Therefore, the source might have experienced a significant variability in intrinsic luminosity as well.

3. Multiwavelength Analysis

J1714+6027 has rich multiwavelength data spanning from X-ray to radio. We report the multiwavelength data and SED fitting of the source in this section.

3.1. Multiwavelength Data

J1714+6027 lies in the Spitzer Space Telescope (M. W. Werner et al. 2004) Extragalactic First Look Survey (XFLS; M. Lacy et al. 2005; D. Fadda et al. 2006) area. The optical (rest-frame UV) spectrum of J1714+6027 was taken using the Palomar 200-inch telescope in 2005, which showed that J1714+6027 is a type 2 quasar at $z = 2.99$ (M. Lacy et al. 2007). This is further confirmed by its near-infrared (rest-frame optical) spectrum taken using the Infrared Telescope Facility (IRTF) in 2007 (M. Lacy et al. 2011), which presented a clear O III emission line. J1714+6027 has a wealth of multiwavelength data, including the photometry data from Dark Energy Spectroscopic Instrument (DESI) Legacy Imaging Surveys DR9 (A. Dey et al. 2019), Sloan Digital Sky Survey (SDSS) DR18, IRTF (M. Lacy et al. 2011), Wide-field Infrared Survey Explorer (WISE; R. M. Cutri et al. 2021), Spitzer (M. Lacy et al. 2005; D. Fadda et al. 2006; D. T. Frayer et al. 2006; M. Lacy et al. 2011), Herschel (M. Lacy et al. 2011), Very Large Array (VLA; J. J. Condon et al. 2003), Giant Metrewave Radio Telescope (GMRT; T. Garn et al. 2007), and the X-ray data reported in this work. We list the multiwavelength data of J1714+6027 in Table 3.

Table 3
Multiwavelength Photometries of J1714+6027

Band	Flux Density
2–10 keV[a] (10^{-14} erg cm^{-2} s^{-1})	3.36 ± 0.44
0.5–2 keV[a] (10^{-14} erg cm^{-2} s^{-1})	1.58 ± 0.22
6 keV[b] (10^{-6} mJy)	1.74 ± 0.23
1.25 keV[b] (10^{-6} mJy)	4.36 ± 0.61
DESI Image g (AB mag)	21.77 ± 0.02
DESI Image r (AB mag)	21.20 ± 0.02
DESI Image z (AB mag)	20.49 ± 0.02
SDSS u (AB mag)	>23.38
SDSS g (AB mag)	21.95 ± 0.07
SDSS r (AB mag)	21.49 ± 0.07
SDSS i (AB mag)	21.02 ± 0.07
SDSS z (AB mag)	21.35 ± 0.38
IRTF H (AB mag)	19.69 ± 0.09
Spitzer 3.6 μm (μJy)	178 ± 19
Spitzer 4.5 μm (μJy)	248 ± 26
Spitzer 5.8 μm (μJy)	495 ± 55
Spitzer 8.0 μm (mJy)	1.08 ± 0.11
WISE 3.4 μm (μJy)	144 ± 5
WISE 4.6 μm (μJy)	266 ± 9
WISE 12 μm (mJy)	2.15 ± 0.08
WISE 22 μm (mJy)	6.29 ± 0.50
Spitzer 24 μm (mJy)	5.60 ± 0.07
Spitzer 70 μm (mJy)	26.4 ± 5.4
Spitzer 160 μm (mJy)	59.0 ± 20.4
Herschel 250 μm (mJy)	<18
Herschel 350 μm (mJy)	<15
VLA 1.4 GHz (mJy)	1.23 ± 0.06
GMRT 610 MHz (mJy)	2.16 ± 0.25

Notes. We report 1σ flux errors.
[a] The X-ray flux is corrected by the absorption requested by CIGALE.
[b] Converted to CIGALE format following G. Yang et al. (2020), Equation (1).

M. Lacy et al. (2011) performed SED fitting of J1714+6027 using the photometry data from SDSS, IRTF, Spitzer, and Herschel. They used a host galaxy stellar burst component (assuming dual stellar populations), an AGN torus component (assuming a power law with a cutoff at the dust sublimation temperature of 1500 K and a longer wavelength cutoff at $\sim$20 μm), and a cold dust component. M. Lacy et al. (2011) found different source star formation rates (SFRs) using different methods: specifically, they measured an SFR $\sim$ 130 $M_\odot$ yr^{-1} using the UV luminosity and SFR $\sim$ 4000–5000 $M_\odot$ yr^{-1} using the far-infrared and radio luminosity, under the assumption that the emission in these bands is dominated by stellar emission. The authors argued that the anomalously huge SFR derived from the far-infrared and radio emission suggests that the flux in these two bands is heavily dominated by the AGN torus. This is also suggested by the lack

of polycyclic aromatic hydrocarbon features in the source mid-infrared 5–38 μm spectrum observed by Spitzer, as well as from the high dust temperature ∼135 K obtained from the SED fitting (M. Lacy et al. 2011).

3.2. SED Fitting

Type 2 quasars constitute a less biased sample to study the properties of the host galaxy of AGN, as their rest-frame optical spectra are dominated by their host galaxies rather than the central nucleus. J1714+6027 is well suited for such a study thanks to its wealth of multiwavelength data available. We performed our SED fitting using the Code Investigating GALaxy Emission (CIGALE) code (D. Burgarella et al. 2005; S. Noll et al. 2009; M. Boquien et al. 2019), which has been widely used to model the physical properties of galaxies with or without an active nucleus (e.g., T. Wang et al. 2019; J. Florez et al. 2020; S. Salim & D. Narayanan 2020; V. A. Masoura et al. 2021; R. Shirley et al. 2021; J. E. Thorne et al. 2021; P. Arrabal Haro et al. 2023; G. Yang et al. 2023). The X-ray data can be used to better constrain the AGN contribution to the rest-frame UV/optical spectrum using the well-established $\alpha_{\rm OX}$ relation (e.g., A. T. Steffen et al. 2006; D. W. Just et al. 2007; E. Lusso & G. Risaliti 2017). Therefore, we used the most updated version of CIGALE v2022.1, which included an X-ray module to better constrain the contribution from AGN to the entire spectrum (G. Yang et al. 2020, 2022). The new version of CIGALE also updated the AGN model to account for a clumpy two-phase torus.

We followed the CIGALE configuration used in G. Yang et al. (2020, 2022) when analyzing J1714+6027. The model includes a stellar emission module, a Galactic dust emission module, and an AGN module. In the stellar emission component, we adopt a delayed star formation history (SFH), `sfhdelayed`, and a single stellar population (SSP) assuming the G. Bruzual & S. Charlot (2003) model, `bc03`. The nebular templates are based on A. K. Inoue (2011). We adopt the Galactic dust attenuation (GDA) module, `dustatt_calzleit` (D. Calzetti et al. 2000; C. Leitherer et al. 2002), and the dust emission `dl2014` module (B. T. Draine et al. 2014). The AGN emission is modeled by `SKIRTOR` (M. Stalevski et al. 2012, 2016). The X-ray luminosity is connected to the accretion disk 2500 Å luminosity through $\alpha_{\rm OX}$.

The SED with the best-fit models is plotted in Figure 5. We note that the AGN emission dominates the entire spectrum of J1714+6027, except for the rest-frame UV/optical band, which is dominated by stellar emission from the host galaxy. This is because of the obscuration along the line of sight of the AGN. The best-fit physical properties of the AGN and its host galaxy of J1714+6027 are presented in Table 4.

The detailed fitting strategy is discussed in Appendix B, where we report the parameters used when fitting the SED in Table 6.

4. Discussion

We discuss the X-ray and multiwavelength variability of the source in Sections 4.1 and 4.2. We then discuss the potential origin of the obscuration of the source observed in 2011 and 2021 in Section 4.3. We discuss the SED shape of the source in Sections 4.4 and 4.5. The source is an obscured hyperluminous IR galaxy, which is further discussed in Section 4.6. The source has a huge SFR and stellar mass, which is discussed in Section 4.7.

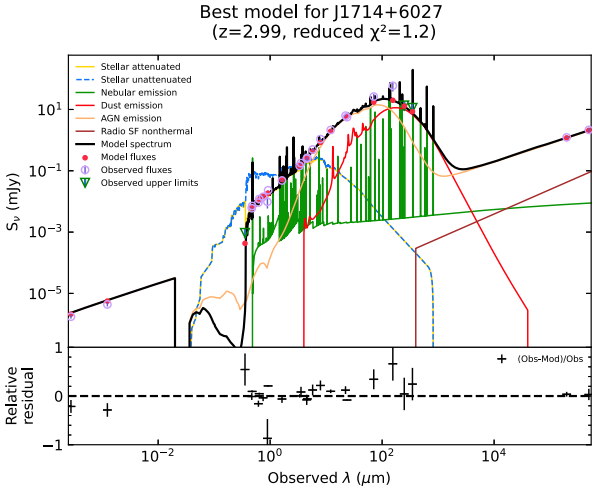

Figure 5. Best-fit SED fitting result from CIGALE and relative residual. The line styles for each module are listed in the key. Relative residual is defined as (`Obs`–`Mod`)/`Obs`, where `Obs` is the observation data and `Mod` is the model prediction.

Table 4
Bayesian-like Estimated Values of the Physical Properties of J1714+6027 Fitted with CIGALE

Property	CIGALE	M. Lacy et al. (2011)	Unit
$\chi^2_{\rm red}$	1.2	4.1	
SFR	1280 ± 77	130–5130	$M_\odot\ {\rm yr}^{-1}$
$L_{\rm AGN}$[a]	3.5 ± 0.2	2.5	$10^{13}\ L_\odot$
$L_{\rm stellar}$	1.6 ± 0.1	…	$10^{13}\ L_\odot$
$M_{\rm star}$	1.1 ± 0.2	2.5	$10^{12}\ M_\odot$
$M_{\rm dust}$[b]	<12	0.1	$10^{8}\ M_\odot$
$M_{\rm gas}$	6.5 ± 1.3	…	$10^{11}\ M_\odot$
$M_{\rm gas,mo}$[c]	…	<2.8	$10^{10}\ M_\odot$
$\alpha_{\rm OX}$	-1.63 ± 0.05	…	
$\rm RL_{30\ deg}$[d]	9.9 ± 0.6	…	

Notes.
[a] The sum of the observed AGN disk and dust reemitted luminosity.
[b] The mass of the dust in the host galaxy.
[c] Molecular gas mass derived converted from CO (1–0) luminosity of the source measured using Extended Very Large Array.
[d] Radio loudness at 30° inclination.

4.1. X-Ray Variability

AGN are variable by definition (e.g., M.-H. Ulrich et al. 1997). X-ray variability has been found in AGN in different timescales from seconds to years (e.g., A. C. Fabian et al. 2009; F. Vagnetti et al. 2011; G. Yang et al. 2016; R. Middei et al. 2017; M. Paolillo et al. 2023). However, simultaneous studies of X-ray flux and spectral shape variability have been performed on a limited number of high-z quasars. J1714+6027 was found to be variable in its flux, column density, and intrinsic luminosity. In this section, we perform comprehensive simulations to further confirm the variability found in J1714+6027.

Due to the limited number of source net counts of the 2011 observation, we performed a set of simulations to validate the X-ray variability found between the 2011 and 2021 observations. In detail, we simulated 10,000 spectra using the exposure

and response files from the 2011 observation assuming that the source properties were measured using the phenomenological model in 2021. In detail, we sample from the full covariance associated with the fits of the 2011 observation using the `AllModels.simpars` function in PyXspec. We then fit each spectrum using the same model used to fit the 2011 observation with a photon index fixed at $\Gamma = 1.45$. Therefore, if a nonnegligible fraction of the best-fit results of the simulations were found to fall in the heavily obscured regime as measured in the 2011 observation, one could not confirm that the source experienced significant variability, and instead could assume that the heavily obscured measurement was due to the low photon statistics of the 2011 spectrum.

The median net count of the 10,000 simulated spectra is 10 counts, which is a little less than the 12 counts measured in the 2011 observation. The median 2–10 keV flux of the 10,000 simulated observations is $F_{2-10} = 4.8 \times 10^{-14}$ erg cm^{-2} s^{-1}, which is consistent with the input $F_{2-10} = 4.6 \times 10^{-14}$ erg cm^{-2} s^{-1} flux. We note that a fraction of 0.7% of the simulated spectrum presents a flux falling in the range of 2–10 keV flux range measured in 2011 within 1σ confidence level, e.g., $F_{2-10} = 0.8$–3.2×10^{-13} erg cm^{-2} s^{-1}. The median column density of the 10,000 simulated spectra is $N_{\rm H,Z} = 6.9 \times 10^{22}$ cm^{-2}. We note a fraction of 1.4% the simulated spectra having column densities falling in the range of the column density range measured in 2011 within the 1σ confidence level, i.e., $N_{\rm H,Z} = (5.6$–$16.5) \times 10^{23}$ cm^{-2}. The median intrinsic 2–10 keV luminosity of the 10,000 simulated spectra is $L_{2-10} = 1.9 \times 10^{45}$ erg s^{-1}, which is consistent with the input $L_{2-10} = 1.8 \times 10^{45}$ erg s^{-1} luminosity. We note a fraction of 0.3% of the simulated spectra having intrinsic 2–10 keV luminosity falling in the range of the intrinsic 2–10 keV luminosity range measured in 2011 within the 1σ confidence level, i.e., $N_{\rm H,Z} = (5.2$–$13.4) \times 10^{45}$ erg s^{-1}.

We plot the distributions of the 2–10 keV flux, column density, and luminosity measured in the 10,000 simulations in Figure 6. Therefore, the 2011 measured source flux, column density, and intrinsic luminosity are not consistent with those measured in the 2021 observations at the $\sim 2\sigma$–3σ confidence level.

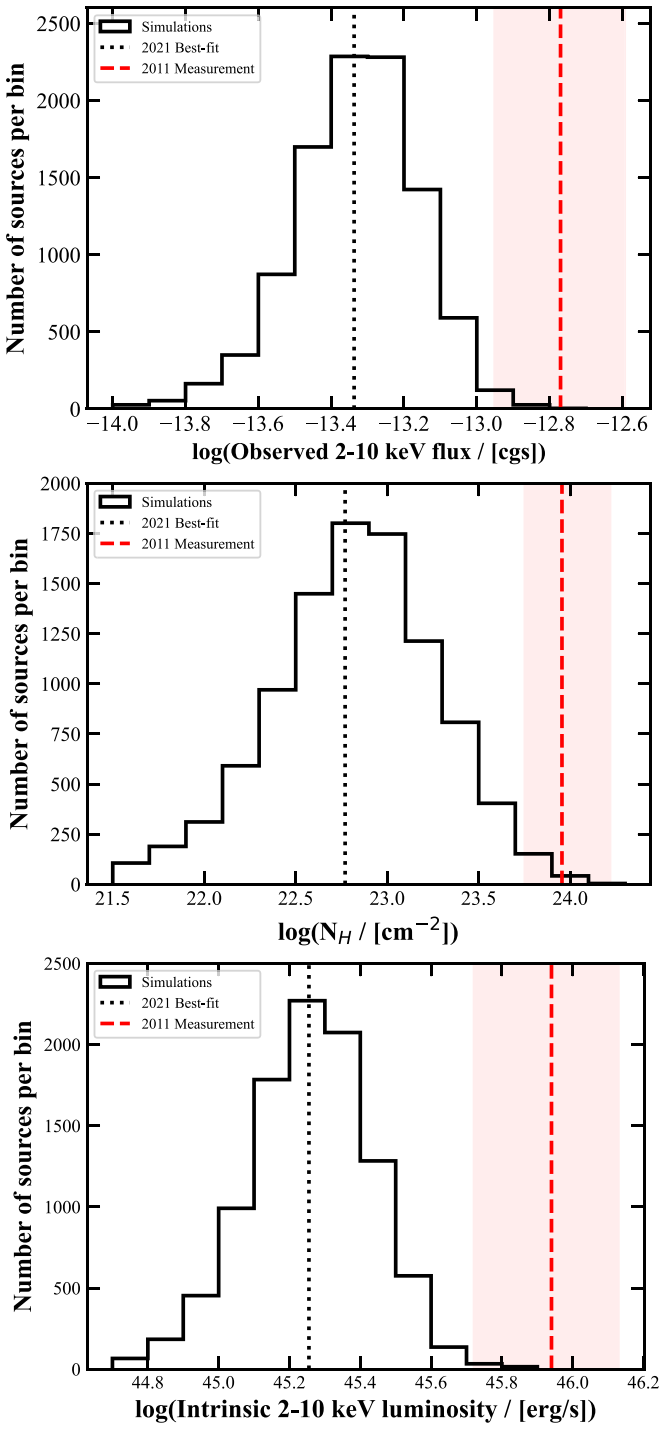

Figure 6. Distributions of the 2–10 keV flux, column density, and 2–10 keV intrinsic luminosity measured in the 10,000 simulations. The black dotted line shows the 2021 best-fit source properties. The red dashed line and the red shaded area show the 2011 measured source properties and their 1σ uncertainty, respectively.

4.2. Multiwavelength Variability

J1714+6027 presented significant X-ray flux variability between the 2011 observation and the 2021 observations. This flux variability is caused by both "line-of-sight" column density variability and intrinsic luminosity variability as shown in Section 2.3. We then searched for potential multiwavelength variability of the source as hinted by the significant X-ray variability. We find a $\sim$0.2 mag difference in the (observed-frame) optical band between the SDSS 2000 observation ($m_r \sim 21.49$ mag) and DESI 2015–2019 observations ($m_r \sim 21.20$ mag). However, the optical flux of the source was consistent between 2009 and 2021 measured by the Palomar Transient Factory (PTF) and Zwicky Transient Facility (ZTF), with a higher average flux than both the SDSS and DESI measurements (e.g., $m_r \sim 21.05$ mag), although a larger flux uncertainty ($\sim$0.2 mag) of PTF and ZTF measurements is noted. Therefore, we argue that no significant flux variability was observed in the optical band between the two X-ray observations in 2011 and 2021. The WISE data also suggest a consistent near-IR flux of the source between 2010 and 2022 within uncertainties, although there was an observation gap between 2011 and 2013. Therefore, significant flux variability of J1714+6027 was only observed in the X-rays rather than in the optical and near-IR. This might be explained by the fact that the observed optical to near-IR (UV and optical in the rest frame) spectra of J1714+6027 are dominated by the emission from the host galaxy (see Figure 5), which is much more stable compared to the nucleus in yearly scale.

4.3. Origin of J1714+6027's Obscuration

The line-of-sight column density of J1714+6027 in 2021 is a few times 10^{22} cm^{-2}. The origin of this obscuration can be

from the gas in the broad-line region (BLR, <0.1 pc), from the dusty gas in the torus (<10 pc), or from the interstellar medium (>kpc) in its host galaxy (see R. C. Hickox & D. M. Alexander 2018, for a review). Recent works (e.g., R. Gilli et al. 2022) have shown that the column density of the interstellar medium (ISM) in the host galaxy increases rapidly toward higher redshift using deep Atacama Large Millimeter/submillimeter Array observations. Their works showed that the ISM could provide an obscuration up to 3×10^{23} cm^{-2} column density at $z \sim 3$, suggesting that the obscuration of J1714+6027 observed in 2021 can be caused by the ISM in its host galaxy considering its high SFR, although we cannot exclude the possibility that the obscuration is caused by the torus.

However, the ISM in the host galaxy alone cannot explain the obscuration found in the 2011 observation of J1714+6027. This is because not only is the column density observed in 2011 larger than 3×10^{23} cm^{-2} but also galactic obscuration should not vary in $\leqslant$2.5 yr (source rest frame). Therefore, the AGN circumnuclear material has to be involved in the obscuration found in 2011. Considering the significant variability found in equal to or less than 10 yr (or 2.5 yr in the source rest frame), the obscuration could be from either the BLR or the torus.

Here we calculate the size of the obscurer by multiplying the velocity of the obscurer ($V_{\rm obs}$) and the variability time (2.5 rest-frame yr). Assuming that the motion of the obscurer is dominated by the gravitational field of the central SMBH, the velocity of the obscurer is $V_{\rm obs} = (GM_{\rm BH}/r)^{1/2}$, where G is the gravitational constant, $M_{\rm BH}$ is the mass of the SMBH, and r is the distance between the obscurer and the central SMBH. If the obscurer is in the BLR, the size of the obscurer is >0.022 pc (assuming that BLR is 0.1 pc away from the SMBH and the variability happened in source rest frame 2.5 yr). If the obscurer is in the torus (assuming at 1 pc away from the SMBH), the obscurer size is >0.007 pc. Here we assume that the SMBH of J1714+6027 is accreting materials less than the Eddington limit. The bolometric luminosity of J1714+6027 is 2.16×10^{47} erg s^{-1} (see Section 4.4), so the BH mass is $M_{\rm BH} \geqslant 1.7 \times 10^9\ M_\odot$. Monitoring the line-of-sight column density variability of the source could provide more information on the properties and distribution of the obscurer surrounding the SMBH. Nevertheless, the fast line-of-sight column density variability suggests a very dynamic environment surrounding the SMBH, and the circumnuclear materials could be clumpy.

4.4. X-Ray to Bolometric Luminosity of AGN

The $K_{\rm X}$-correction, i.e., the relation of 2–10 keV luminosity to bolometric luminosity ($L_{\rm BOL}$), is a significant ingredient to study the energy transfer process in AGN, which was found to significantly depend on the bolometric luminosity but not depend on the redshift (e.g., F. Duras et al. 2020). The $K_{\rm X}$-correction has been widely used to derive the bolometric luminosity of the X-ray-detected AGN. E. Lusso et al. (2012) and F. Duras et al. (2020) derived $K_{\rm X}$ as a function of bolometric luminosity using a sample of X-ray-detected AGN. They found a very similar $K_{\rm X}$–$L_{\rm BOL}$ relation for type 1 AGN, but the $K_{\rm X}$–$L_{\rm BOL}$ relation in the luminous end of the type 2 AGN was not well constrained (Figure 7), due to the lack of a sample of luminous type 2 AGN.

J1714+6027 is a good target for constraining the $K_{\rm X}$–$L_{\rm BOL}$ relation at the luminous end. We used the 2–10 keV intrinsic luminosity of sources in the 2021 observation derived from the `borus` model, which is 1.7×10^{45} erg s^{-1}. As the bolometric luminosity of type 2 AGN cannot be derived directly from integrating the AGN emission components in the SED fitting (from X-ray to optical bands), we computed the bolometric luminosity of J1714+6027 following the method used in E. Lusso et al. (2012) and F. Duras et al. (2020). In their work, the bolometric luminosity of type 2 AGN was derived by scaling the IR (from 1 to 1000 μm) luminosity of the AGN by a factor of 1.9 (F. Pozzi et al. 2007). Therefore, the bolometric luminosity of J1714+6027 is $L_{\rm BOL} = 2.5 \times 10^{47}$ erg s^{-1}. Therefore, the $K_{\rm X}$-correction of J1714+6027 is $K_{\rm X} = 147$.

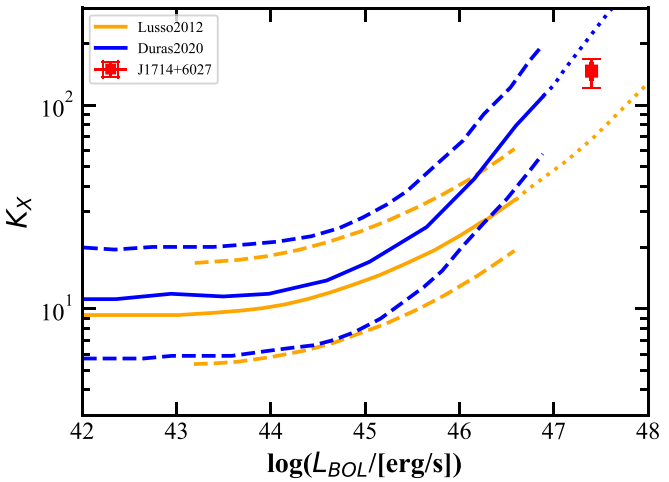

Figure 7. $K_{\rm X}$ as a function of bolometric luminosity of type 2 AGN. The red square is J1714+6027 (the error bar is in 1σ). The orange and blue lines are the measurements (solid) and extrapolation (dotted) derived in E. Lusso et al. (2012) and F. Duras et al. (2020), respectively. The dashed lines correspond to the 1σ spread of the samples used in the two works. The bolometric luminosities of the type 2 AGN in their work span a range from 10^{42} erg s^{-1} to 2×10^{46} erg s^{-1}. Beyond these bolometric luminosities, the $K_{\rm X}$-correction was extrapolated from the measured data following $K_{\rm X} = a[1+(\log(L_{\rm BOL}/L_\odot)/b)^c]$. a, b, c are coefficients that were measured to be constants as a function of the bolometric luminosity.

Figure 7 plots $K_{\rm X}$ as a function of the bolometric luminosity of type 2 AGN derived in E. Lusso et al. (2012) and F. Duras et al. (2020). We note that J1714+6027 has the largest bolometric luminosity among the sources in both of the samples. J1714+6027 lies between the $K_{\rm X}$–$L_{\rm BOL}$ relations extrapolated from the two samples but is closer to the more recent relation derived by F. Duras et al. (2020). It is shown that J1714+6027 is a valuable source to derive the intrinsic $K_{\rm X}$–$L_{\rm BOL}$ relation, but a larger sample of such luminous type 2 quasars is needed to constrain the relation.

The above correlation suggested that the X-ray emission contributes much less at the bright end. We note that the optical-to-bolometric luminosity ratio ($K_{\rm O}$) is nearly a constant as a function of $L_{\rm BOL}$, even at the bright end (F. Duras et al. 2020). Therefore, this might imply that the X-ray emitter, i.e., the corona, might have different physical or geometrical properties in different luminosity regimes (e.g., L. Zappacosta et al. 2020).

4.5. X-Ray to Mid-IR Luminosity

The X-ray emission and mid-IR emission from AGN are strongly correlated owing to the same energy budget. In recent decades, the intrinsic X-ray and mid-IR luminosities of AGN have been explored in different redshift and luminosity scales (e.g., D. Lutz et al. 2004; F. Fiore et al. 2009; P. Gandhi et al. 2009; G. Lanzuisi et al. 2009; D. Asmus et al. 2015;

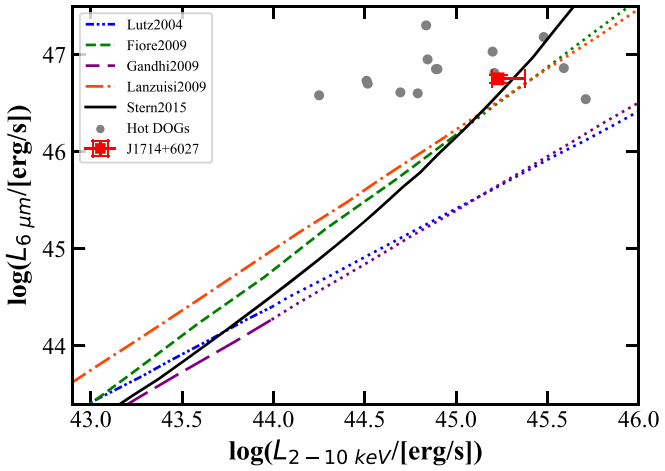

Figure 8. Rest-frame 6 μm AGN luminosity as a function of the 2–10 keV intrinsic luminosity of J1714+6027 (red square) compared with the mid-IR-to-X-ray relation obtained by D. Lutz et al. (2004; blue dotted line), F. Fiore et al. (2009; green short-dashed line), P. Gandhi et al. (2009; purple long-dashed line), G. Lanzuisi et al. (2009; orange dashed–dotted line), and D. Stern (2015; black solid line). The extrapolations of each work to higher luminosities are plotted with dotted lines. Hot DOGs from C. Ricci et al. (2017a), R. J. Assef et al. (2016), F. Vito et al. (2018), and L. Zappacosta et al. (2018b) are plotted as gray circles.

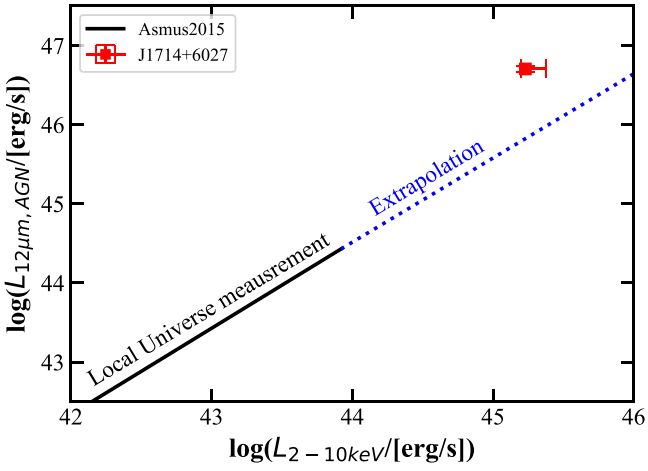

Figure 9. Rest-frame 12 μm AGN luminosity as a function of 2–10 keV intrinsic luminosity of J1714+6027 (red square) and D. Asmus et al. (2015) measurement using a sample of obscured ($22 < \log(N_{\rm H}) < 23$) AGN in the local Universe and its extrapolation to high luminosities (blue dotted line).

D. Stern 2015). Indeed, a strong correlation between the X-ray and mid-IR luminosity was detected. However, such a correlation was found to evolve with AGN luminosities: the X-ray luminosity increases more slowly than the mid-IR luminosity as the AGN luminosity increases (D. Stern 2015; see also Figure 8). This might suggest that there is an evolution of the AGN mid-IR emitter, in which the band is typically dominated by the AGN dusty torus. It is worth mentioning that the correlations obtained by D. Lutz et al. (2004) and P. Gandhi et al. (2009) were both derived from local AGN samples, which could well separate the AGN and host galaxy emissions but only sampled the low-luminosity regime ($L_{2-10\,\rm keV} \leqslant 10^{44}\,\rm erg\,s^{-1}$). F. Fiore et al. (2009) and G. Lanzuisi et al. (2009) sampled more luminous quasars with $L_{2-10\,\rm keV}$ up to $10^{45}\,\rm erg\,s^{-1}$. The brightest quasars with $L_{2-10\,\rm keV}$ up to $10^{46}\,\rm erg\,s^{-1}$ were sampled by D. Stern (2015). But they are not able to resolve the nuclei.

We calculated the rest-frame mid-IR 6 μm and 2–10 keV intrinsic luminosity from the best-fit SED of J1714+6027. The object is well consistent with the correlations derived in F. Fiore et al. (2009), G. Lanzuisi et al. (2009), and D. Stern (2015). It is worth mentioning that the AGN mid-IR luminosity of the sources in their sample can have nonnegligible contamination from the host galaxy even for type 1 AGN (G. Yang et al. 2020). Therefore, F. Fiore et al. (2009), G. Lanzuisi et al. (2009), and D. Stern (2015) might overestimate the mid-IR luminosity of the AGN by including the contribution from the host galaxies. The entire 6 μm luminosity of J1714+6027 is $L_{6\,\mu\rm m,tot} = 6.2 \times 10^{46}\,\rm erg\,s^{-1}$, which is 11% higher than its AGN luminosity ($L_{6\,\mu\rm m,AGN} = 5.6 \times 10^{46}\,\rm erg\,s^{-1}$) as plotted in Figure 8.

D. Asmus et al. (2015) explored the correlation of 12 μm to X-ray luminosity using a sample of mid-IR resolved AGN in the local Universe ($L_{2-10\,\rm keV} \leqslant 10^{44}\,\rm erg\,s^{-1}$). We plot the correlation derived in D. Asmus et al. (2015) with similar column densities ($22 < \log N_{\rm H} < 23$) to what was measured in J1714+6027 in Figure 9. The 12 μm luminosity of J1714+6027 is $L_{12\,\mu\rm m,AGN} = 5.1 \times 10^{46}\,\rm erg\,s^{-1}$. We find a significant offset between the D. Asmus et al. (2015) best-fit correlation and J1714+6027, suggesting an evolution of the AGN mid-IR emitter as found in the correlation of 6 μm to X-ray luminosity.

The evolution of the X-ray-to-mid-IR correlation presented in Figures 8 and 9 might be due to the evolution of the $K_{\rm X}$–$L_{\rm BOL}$ correlation, as the mid-infrared photons are the UV/optical photons reprocessed by the circumnuclear dust.

4.6. J1714+6027 and a Hot, Dust-obscured Galaxy

The total IR (8–1000 μm) luminosity of J1714+6027 is $L_{\rm IR} \sim 2.6 \times 10^{13}\,L_{\odot}$, suggesting that it is an IR hyperluminous galaxy ($L_{\rm IR} = 10^{13}$–$10^{14}\,L_{\odot}$; e.g., P. R. M. Eisenhardt et al. 2012). The peak of the SED of J1714+6027 is at (source rest frame) $\lambda \sim 21$ μm, suggesting that the dust is hot ($T \gg 100$ K, derived with the relation presented in Figure 20 in C. M. Casey et al. 2014). Its SED also presents a significant bump at the IR band, suggesting a large amount of dust inside the torus of the AGN. Therefore, J1714+6027 is an IR hyperluminous, obscured galaxy with a significant amount of dust in the torus.

In the past two decades, a sample of IR hyperluminous, hot, dust-obscured galaxies (DOGs) were discovered (P. R. M. Eisenhardt et al. 2012; J. Wu et al. 2012; C.-W. Tsai et al. 2015), selected using the W1W2 dropout criteria (i.e., these sources are bright in the WISE W3 and W4 bands but are very faint (or not detected) in the W1 and W2 bands). J1714+6027 does not fulfill the definition of hot DOGs, but they share similar IR luminosity and dust temperature. We note that hot DOGs might have stronger IR emission compared with their optical emission, which suggests that hot DOGs have a larger amount of dust in the torus or the central engine is more obscured by the dust. It is worth mentioning that DOGs were selected using the criteria with 24 μm flux density $F_{24\,\mu\rm m} \geqslant 0.3$ mJy and $F_{\nu}(24\,\mu\rm m)/F_{\nu}(R) \geqslant 1000$ (A. Dey et al. 2008). J1714+6027 has a 24 μm flux density $F_{24\,\mu\rm m} = 5.6$ mJy but a little less $F_{\nu}(24\,\mu\rm m)/F_{\nu}(R) \sim 500$, suggesting a lower IR-to-optical flux ratio. Nevertheless, it is worth comparing the X-ray properties of J1714+6027 with those of the hot DOGs.

The intrinsic X-ray luminosities of hot DOGs were found widely spread at similar IR luminosities (see Figure 8; R. J. Assef et al. 2016; C. Ricci et al. 2017a; F. Vito et al. 2018; L. Zappacosta et al. 2018b), with a large fraction of them

being intrinsically X-ray weak compared with other AGN (especially type 1 AGN) at similar luminosities. However, it is worth noting that the obscurations of half of the hot DOGs in the C. Ricci et al. (2017a) sample (where most of the intrinsically X-ray-weak hot DOGs were discovered) are derived from the empirical equation between $E(B-V)$ and column density (see Equation (1) in their paper). This method can lead to column density with large uncertainty, and thus an uncertain intrinsic X-ray luminosity, especially in the heavily obscured regime. J1714+6027 presents a similar X-ray-to-mid-IR correlation to that of other unobscured AGN (Section 4.5) and is indistinguishable from the hot DOG sample regarding the X-ray-to-mid-IR relation.

Hot DOGs are thought to be powered by highly obscured AGN ($N_{\rm H} \gg 10^{23}\,{\rm cm}^{-2}$), with many being CT (e.g., R. J. Assef et al. 2016), although the X-ray obscuration measurements of the current hot DOG sample are highly uncertain (E. Piconcelli et al. 2015; C. Ricci et al. 2017a; F. Vito et al. 2018; L. Zappacosta et al. 2018a). J1714+6027 is indeed less obscured in 2021 compared with hot DOGs. However, it is worth noting that J1714+6027 is an obscuration variable and was much more obscured in 2011. Therefore, J1714+6027 is indistinguishable from the hot DOG sample regarding the X-ray obscuration.

Therefore, we found that although J1714+6027 does not follow the definition of hot DOGs, it shares many similar properties with hot DOGs. There might be an evolutionary sequence of dust-obscured, IR-luminous sources as proposed in R. J. Assef et al. (2022).

4.7. SFR of the Host Galaxy of AGN in the Early Universe

The AGN feedback is thought to be involved in shaping the star-forming process of their host galaxies (e.g., G. L. Granato et al. 2004; T. Di Matteo et al. 2005; A. C. Fabian 2012; P. Madau & M. Dickinson 2014). Type 2 quasars are great samples to extract the physical properties of the stellar population in the host galaxy of AGN, as the stellar emission from the host galaxy is overwhelmed by the nuclei emission in type 1 AGN. Huge SFR ($\sim$1280 $M_\odot\,{\rm yr}^{-1}$) and stellar mass ($M_{\rm star} \sim 1.1 \times 10^{12}\,M_\odot$) were found in the host galaxy of J1714+6027, which were rare to be found in AGN even at this redshift (e.g., G. Lanzuisi et al. 2017). E. Pouliasis et al. (2022) studied the host galaxy properties of a sample of X-ray-detected, high-redshift ($z \geqslant 3.5$) AGN. J1714+6027 is in the stellar active and massive end of the E. Pouliasis et al. (2022) sample, whose median SFR is $\approx$240 $M_\odot\,{\rm yr}^{-1}$ and median stellar mass is $M_{\rm star} \sim 5.6 \times 10^{10}\,M_\odot$.The SFR as a function of the stellar mass of J1714+6027 is consistent with the E. Pouliasis et al. (2022) sample as shown in Figure 10.

The main-sequence (MS) star-forming galaxies also present a strong correlation between SFR and stellar mass (e.g., C. Schreiber et al. 2015). E. Pouliasis et al. (2022) found that a large fraction of the high-redshift AGN in their sample presented enhanced SFR compared with the high-redshift (median $z \sim 3.7$) MS star-forming galaxies with similar stellar mass (C. Schreiber et al. 2015). However, the SFR is not enhanced by AGN compared with MS star-forming galaxies with $M_{\rm star} > 10^{12}\,M_\odot$, which is also evident by J1714+6027 (Figure 10). This might suggest that the gas reservoir in the host galaxy rather than the presence of AGN regulates the SFR in the massive end of galaxies.

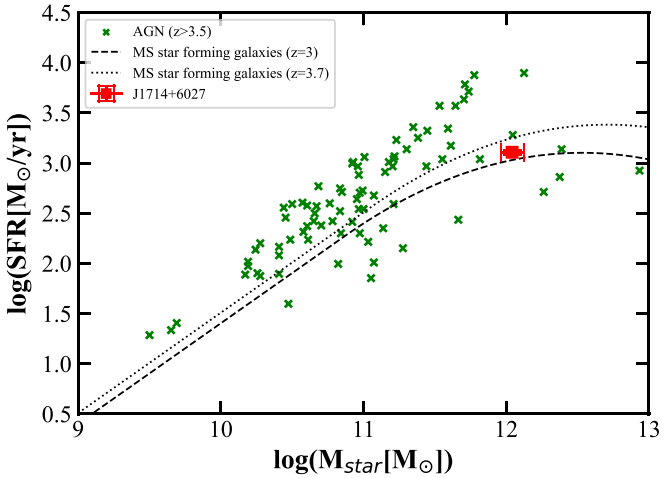

Figure 10. SFR as a function of stellar mass of J1714+6027 (red square) and $z \geqslant 3.5$ AGN (median redshift of 3.7) measured in E. Pouliasis et al. (2022). The dashed and dotted lines represent the SFR and stellar mass correlations of $z = 3$ and $z = 3.7$ MS star-forming galaxies derived in C. Schreiber et al. (2015), respectively.

5. Conclusions

J1714+6027 is a type 2 quasar at $z = 2.99$. Its 2011 shallow X-ray observation suggested that the source is a candidate CT quasar, which was then reviewed with deep NuSTAR and XMM-Newton observations in the year 2021. In this work, we analyzed its recent X-ray data and performed an SED fitting of the source thanks to its great multiwavelength data. We find the following:

1. The source was found to be a candidate CT quasar with a column density of $N_{\rm H,Z,2011} = 9.5^{+17.2}_{-5.9} \times 10^{23}\,{\rm cm}^{-2}$. The recent deep NuSTAR and XMM-Newton observations showed that the source is less obscured with a column density of $N_{\rm H,Z,2021} = 5.9^{+4.9}_{-3.6} \times 10^{22}\,{\rm cm}^{-2}$.
2. The source presented significant variability in its X-ray flux, obscuration, and intrinsic luminosities at 2σ–3σ confidence level in 2.5 yr (in source rest frame).
3. The source was not found to vary as significantly in the optical and near-IR bands as we observed in the X-rays. This might be because the source emission in the optical and near-IR bands is dominated by the host galaxy.
4. We explored the origin of the X-ray obscuration of the source. The previously measured heavy obscuration in the year 2011 can be from either the AGN BLR or the AGN torus. We estimated that the size of the obscurer is >0.022 pc if it is in the BLR or is >0.007 pc if it is in the torus. The recently measured lower obscuration of the source in the year 2021 can originate from the AGN torus and its host galaxy.
5. The source is an extremely luminous type 2 quasar with a bolometric luminosity of $L_{\rm BOL} = 2.5 \times 10^{47}\,{\rm erg\,s}^{-1}$. The $K_{\rm X}$–$L_{\rm BOL}$ correlation is less constrained in the bright end of the bolometric luminosity. J1714+6027 has the largest bolometric luminosity among the sources in both the E. Lusso et al. (2012) and F. Duras et al. (2020) samples. We found that J1714+6027 lies between the $K_{\rm X}$–$L_{\rm BOL}$ relations extrapolated from the two samples but is closer to the more recent F. Duras et al. (2020) $K_{\rm X}$–$L_{\rm BOL}$ relation. A larger sample of bright AGN is needed to constrain the correlation at the bright end, which will also

be vital to understanding the AGN corona at different luminosities.

6. We found that the source followed the evolution of the correlation between X-ray luminosity and mid-IR luminosity, where a much higher mid-IR luminosity is found for high X-ray luminosity sources. This might be due to the evolution of the K_X–L_{BOL} correlation.
7. The source is an IR hyperluminous, obscured galaxy with a significant amount of hot dust in its torus. We found that J1714+6027 shares many similar properties with hot DOGs.
8. The source has a huge SFR ($\sim 1280\, M_\odot\, \mathrm{yr}^{-1}$) and stellar mass ($M_{\mathrm{star}} \sim 1.1 \times 10^{12}\, M_\odot$). Its SFR–stellar mass correlation is consistent with what was found in other $z > 3.5$ AGN. The correlation is also consistent with what was found in the $z = 3$ MS star-forming galaxies, suggesting that the existence of an active nucleus does not enhance the SFR.

Acknowledgments

X.Z. thanks the anonymous referee for the very helpful comments on the manuscript. X.Z. acknowledges NASA funding under contract No. 80NSSC20K0043. X.Z. thanks Yue Shen and Roberto Assef for their very helpful comments on the paper. X.Z. thanks Qian Yang, Guang Yang, and Mingyang Zhuang for the helpful discussion on the SED fitting. IEL acknowledges support from the Cassini Fellowship program at INAF-OAS and the European Union's Horizon 2020 research and innovation program under Marie Sklodowska-Curie grant agreement No. 860744 "Big Data Applications for Black Hole Evolution Studies" (BiD4BESt). We thank Karl Foster and Murry Brightman and the NuSTAR observation planning team for their help in designing the observation plan and scheduling the observations.

This work has made use of data from the NuSTAR mission, a project led by the California Institute of Technology, managed by the Jet Propulsion Laboratory, and funded by the National Aeronautics and Space Administration. This research has made use of the NuSTARDAS jointly developed by the ASI Science Data Center (ASDC, Italy) and the California Institute of Technology (USA). This research has made use of data and software provided by the High Energy Astrophysics Science Archive Research Center (HEASARC), which is a service of the Astrophysics Science Division at NASA/GSFC and the High Energy Astrophysics Division of the Smithsonian Astrophysical Observatory. This work is based on observations obtained with XMM-Newton, an ESA science mission with instruments and contributions directly funded by ESA Member States and NASA. This work makes use of the data from SDSS. Funding for the SDSS has been provided by the Alfred P. Sloan Foundation, the US Department of Energy Office of Science, and the Participating Institutions. This work is partly based on the data from WISE, which is a joint project of the University of California, Los Angeles, and the Jet Propulsion Laboratory/California Institute of Technology. The DESI Legacy Imaging Surveys consist of three individual and complementary projects: the Dark Energy Camera Legacy Survey (DECaLS), the Beijing–Arizona Sky Survey (BASS), and the Mayall z-band Legacy Survey (MzLS). DECaLS, BASS, and MzLS together include data obtained, respectively, at the Blanco telescope, Cerro Tololo Inter-American Observatory, NSF's NOIRLab; the Bok telescope, Steward Observatory, University of Arizona; and the Mayall telescope, Kitt Peak National Observatory, NOIRLab. NOIRLab is operated by the Association of Universities for Research in Astronomy (AURA) under a cooperative agreement with the National Science Foundation. Pipeline processing and analyses of the data were supported by NOIRLab and the Lawrence Berkeley National Laboratory (LBNL). Legacy Surveys was supported by the Director, Office of Science, Office of High Energy Physics of the US Department of Energy; the National Energy Research Scientific Computing Center, a DOE Office of Science User Facility; the US National Science Foundation, Division of Astronomical Sciences; and the National Astronomical Observatories of China, the Chinese Academy of Sciences, and the Chinese National Natural Science Foundation. LBNL is managed by the Regents of the University of California under contract to the US Department of Energy. This work is based in part on archival data obtained with the Spitzer Space Telescope, which was operated by the Jet Propulsion Laboratory, California Institute of Technology under a contract with NASA. Support for this work was provided by NASA. Herschel is an ESA space observatory with science instruments provided by European-led Principal Investigator consortia and with important participation from NASA. The National Radio Astronomy Observatory is a facility of the National Science Foundation operated under cooperative agreement by Associated Universities, Inc. We thank the staff of the GMRT that made these observations possible. GMRT is run by the National Center for Radio Astrophysics of the Tata Institute of Fundamental Research.

Appendix A
X-Ray Spectral Analysis of the Sources near J1714+6027

We analyze the XMM-Newton spectra of three sources near J1714+6027, which are J171430+602722, J171430+602635, and J171425+602928. We extracted the XMM-Newton spectra of the two sources following Section 2.1.2. The two sources are point sources in their optical images, so we fit their spectra with the phenomenological model as described in Section 2.2.1 assuming that they are AGN. They do not have redshift information, so we assume that they are at $z = 0$. We found that their spectra can be well fitted with a simple power-law model, without the need for an additional absorption component besides the galactic absorption. Therefore, we fit the spectra only with a simple power-law model in case we overfit the data. The best-fit results are listed in Table 5.

J171425+602928 is bright in NuSTAR, so we analyze its NuSTAR (3–24 keV) spectrum as well. We found that its best-fit photon index is $\Gamma = 1.75^{+0.35}_{-0.37}$ and 2–10 keV flux is $F_{2-10} = 1.3^{+0.2}_{-0.3} \times 10^{-13}\,\mathrm{erg\,cm^{-2}\,s^{-1}}$, which is different from what we measured from its XMM-Newton spectra. We note that this might be due to the variability of the source. We found that J171425+602928 presented evidence for intra-observation net count rate variability during the XMM-Newton observations at the $>5\sigma$ level. The net count rate varied by up to 5 times during the XMM-Newton observations. As XMM-Newton observation only overlapped with the NuSTAR observation by 30%, the source might have higher flux in the rest of the NuSTAR observation when the source was not observed by XMM-Newton. Nevertheless, detailed variability and spectral analysis are beyond the scope of this paper.

Table 5
Summary of Best Fit of XMM-Newton Spectra of J171430+602722, J171430+602635, and J171425+602928 Using the Phenomenological Model

	J171430+602722	J171430+602635	J171425+602928
C/dof	20/33	20/29	183/171
Γ	$1.73^{+0.20}_{-0.21}$	$1.90^{+0.23}_{-0.25}$	$2.22^{+0.06}_{-0.07}$
$F_{0.5-2}$ [a]	$1.1^{+0.2}_{-0.1}$	$1.0^{+0.1}_{-0.1}$	$8.2^{+0.3}_{-0.4}$
F_{2-10} [b]	$2.1^{+0.6}_{-0.6}$	$1.4^{+0.5}_{-0.5}$	$7.3^{+0.7}_{-0.7}$

Notes.
[a] 0.5–2 keV flux in 10^{-14} erg cm^{-2} s^{-1}.
[b] 2–10 keV flux in 10^{-14} erg cm^{-2} s^{-1}.

Appendix B
CIGALE Setup

We set up the CIGALE parameters following what was used in G. Yang et al. (2022) when modeling mid-IR-detected type 2 AGN. Most of the parameters were chosen to be the default values to reduce the degeneracy, besides the parameters discussed below. The fitting parameter values in Cigale are presented in Table 6.

When modeling the stellar emission, we selected 1 and 2 Gyr for the age of the main stellar population in the galaxy, as the age of J1714+6027 is 2.1 Gyr at $z = 2.99$. We found a huge stellar population metallicity of $Z_{\rm gas} = 0.051$ (the maximum allowed value in CIGALE), which is in agreement with the best-fit stellar age $t = 2$ Gyr, suggesting a mutual galaxy.

When modeling the dust emission, we select the `dl2014` model (B. T. Draine et al. 2014) rather than the default `dale2014` model (D. A. Dale et al. 2014). The `dl2014` model has a more complex dust emission model (see discussion in M. Boquien et al. 2019) and thus has more flexibility in the allowed parameter space compared with the `dale2014` model. We found that the `dale2014` model cannot well fit the overall spectral shape of J1714+6027 with a best-fit reduced χ^2 of 2.9. We note that the property of the dust of the host galaxy is loosely constrained, due to the lack of data (and measurements) at rest-frame mid-IR to far-IR, where the dust component starts to dominate.

The best-fit results suggest that the AGN is observed through a face-on direction and possess a small covering factor torus as suggested in the X-ray spectral analysis of J1714+6027.

As CIGALE uses a power-law model when fitting the X-ray spectra and requested the flux to be absorption corrected, we used the fluxes of the intrinsic power law derived from the `borus` model as the input data to CIGALE. When modeling the X-ray component, which should be dominated by the AGN rather than the X-ray binaries in the host galaxy, we fixed the photon index of the source at $\Gamma = 1.60$ as we derived from the X-ray spectral fitting. We allow the $\alpha_{\rm OX}$ parameter to be free to vary. The radio emission is also dominated by the AGN. We allow the optical radio-loudness ($\rm RL_{30\ deg} = L_{\nu,5\ GHz}/L_{\nu,2500\ Å}$, where $L_{\nu,2500\ Å}$ is the AGN 2500 Å intrinsic disk luminosity measured at the inclination angle $i = 30°$) free to vary when fitting.

The dust mass of the host galaxy is not constrained. The best-fit radio-loudness is $\rm RL_{30\ deg} = 10$, suggesting that the source is radio-quiet.

Table 6
Fitting Parameter Values in CIGALE

Module	Parameter	Values
SFH	e-folding time, τ (Gyr)	1, **2**, 3
	Stellar age, t (Gyr)	1, **2**
SSP	Initial mass function (IMF)	G. Chabrier (2003)
	Metallicity, $Z_{\rm gas}$	0.02, 0.05
GDA	Young population	0.1, 0.2, 0.3
	Power-law slope	0, –0.2, –0.4
Nebula	Ionization parameter (log' U)	–3
	Gas metallicity ($Z_{\rm gas}$)	0.011
Dust	Minimum radiation field (Umin)	1, 10, 30, **50**
	Power-law slope, α	1, **2**, 3
	Fraction illuminated	0.5, 0.7, 0.9
AGN	Optical depth at 9.7 μm	3, **7**
	Inclination angle, i	20°, 90°
	Angle between the equatorial plane and the edge of the torus, oa	40°, 80°
	Disk type	M. Schartmann et al. (2005)
	Polar direction $E(B-V)$	0.09, 0.4
	Polar dust temperature (K)	100, **1000**, 5000
	Disk slop modification, δ	0.36
	AGN fraction ($\rm frac_{AGN}$)	0.5, 0.7, 0.9
X-ray	Photon index	1.6
	$\alpha_{\rm OX}$	–1.5, –1.6, –1.7
	Maximum allowed deviation of $\alpha_{\rm OX}$ from the empirical relation	0.2
Radio	Radio-loudness	5, **10**, 15
	AGN radio slope	0.6

Note. The best-fit values are shown in bold.

ORCID iDs

Xiurui Zhao https://orcid.org/0000-0002-7791-3671
Stefano Marchesi https://orcid.org/0000-0001-5544-0749
Marco Ajello https://orcid.org/0000-0002-6584-1703
Francesca Civano https://orcid.org/0000-0002-2115-1137
Roberto Gilli https://orcid.org/0000-0001-8121-6177
Giorgio Lanzuisi https://orcid.org/0000-0001-9094-0984
Iván E. López https://orcid.org/0000-0003-4687-8401
Peter G. Boorman https://orcid.org/0000-0001-9379-4716
Ross Silver https://orcid.org/0000-0001-6564-0517
Nuria Torres-Albà https://orcid.org/0000-0003-3638-8943
Andrealuna Pizzetti https://orcid.org/0000-0001-6412-2312

References

Anders, E., & Grevesse, N. 1989, GeCoA, 53, 197
Annuar, A., Gandhi, P., Alexander, D. M., et al. 2015, ApJ, 815, 36
Arnaud, K. A. 1996, adass, 101, 17
Arrabal Haro, P., Dickinson, M., Finkelstein, S. L., et al. 2023, Natur, 622, 707
Asmus, D., Gandhi, P., Honig, S. F., Smette, A., & Duschl, W. J. 2015, MNRAS, 454, 766
Assef, R. J., Bauer, F. E., Blain, A. W., et al. 2022, ApJ, 934, 101
Assef, R. J., Walton, D. J., Brightman, M., et al. 2016, ApJ, 819, 111
Balokovic, M., Brightman, M., Harrison, F. A., et al. 2018, ApJ, 854, 42
Boorman, P. G., Torres-Albà, N., Annuar, A., et al. 2024, FrASS, 11, 1335459
Boquien, M., Burgarella, D., Roehlly, Y., et al. 2019, A&A, 622, A103
Bruzual, G., & Charlot, S. 2003, MNRAS, 344, 1000
Buchner, J., Georgakakis, A., Nandra, K., et al. 2015, ApJ, 802, 89

Burgarella, D., Buat, V., & Iglesias-Paramo, J. 2005, MNRAS, 360, 1413
Calzetti, D., Armus, L., Bohlin, R. C., et al. 2000, ApJ, 533, 682
Casey, C. M., Narayanan, D., & Cooray, A. 2014, PhR, 541, 45
Cash, W. 1979, ApJ, 228, 939
Chabrier, G. 2003, ApJL, 586, L133
Condon, J. J., Cotton, W. D., Yin, Q. F., et al. 2003, AJ, 125, 2411
Cutri, R. M., Wright, E. L., Conrow, T., et al. 2021, VizieR Online Data Catalog
Daddi, E., Alexander, D. M., Dickinson, M., et al. 2007, ApJ, 670, 173
Dale, D. A., Helou, G., Magdis, G. E., et al. 2014, ApJ, 784, 83
Delvecchio, I., Gruppioni, C., Pozzi, F., et al. 2014, MNRAS, 439, 2736
Dey, A., Schlegel, D. J., Lang, D., et al. 2019, AJ, 157, 168
Dey, A., Soifer, B. T., Desai, V., et al. 2008, ApJ, 677, 943
Di Matteo, T., Springel, V., & Hernquist, L. 2005, Natur, 433, 604
Draine, B. T., Aniano, G., Krause, O., et al. 2014, ApJ, 780, 172
Duras, F., Bongiorno, A., Ricci, F., et al. 2020, A&A, 636, A73
Eisenhardt, P. R. M., Wu, J., Tsai, C.-W., et al. 2012, ApJ, 755, 173
Fabian, A. C. 2012, ARA&A, 50, 455
Fabian, A. C., Zoghbi, A., Ross, R. R., et al. 2009, Natur, 459, 540
Fadda, D., Marleau, F. R., Storrie-Lombardi, L. J., et al. 2006, AJ, 131, 2859
Fiore, F., Puccetti, S., Brusa, M., et al. 2009, ApJ, 693, 447
Florez, J., Jogee, S., Sherman, S., et al. 2020, MNRAS, 497, 3273
Frayer, D. T., Fadda, D., Yan, L., et al. 2006, AJ, 131, 250
Gandhi, P., Horst, H., Smette, A., et al. 2009, A&A, 502, 457
Garn, T., Green, D. A., Hales, S. E. G., Riley, J. M., & Alexander, P. 2007, MNRAS, 376, 1251
Gilli, R., Comastri, A., & Hasinger, G. 2007, A&A, 463, 79
Gilli, R., Norman, C., Calura, F., et al. 2022, A&A, 666, A17
Gilli, R., Su, J., Norman, C., et al. 2011, ApJL, 730, L28
Granato, G. L., De Zotti, G., Silva, L., Bressan, A., & Danese, L. 2004, ApJ, 600, 580
HI4PI Collaboration, Ben Bekhti, N., Flöer, L., et al. 2016, A&A, 594, A116
Hickox, R. C., & Alexander, D. M. 2018, ARA&A, 56, 625
Inoue, A. K. 2011, MNRAS, 415, 2920
Jansen, F., Lumb, D., Altieri, B., et al. 2001, A&A, 365, L1
Just, D. W., Brandt, W. N., Shemmer, O., et al. 2007, ApJ, 665, 1004
Lacy, M., Petric, A. O., Martínez-Sansigre, A., et al. 2011, AJ, 142, 196
Lacy, M., Petric, A. O., Sajina, A., et al. 2007, AJ, 133, 186
Lacy, M., Wilson, G., Masci, F., et al. 2005, ApJS, 161, 41
Lanzuisi, G., Civano, F., Marchesi, S., et al. 2018, MNRAS, 480, 2578
Lanzuisi, G., Delvecchio, I., Berta, S., et al. 2017, A&A, 602, A123
Lanzuisi, G., Gilli, R., Cappi, M., et al. 2019, ApJL, 875, L20
Lanzuisi, G., Piconcelli, E., Fiore, F., et al. 2009, A&A, 498, 67
Leitherer, C., Li, I. H., Calzetti, D., & Heckman, T. M. 2002, ApJS, 140, 303
Lightman, A. P., & White, T. R. 1988, ApJ, 335, 57
Lusso, E., Comastri, A., Simmons, B. D., et al. 2012, MNRAS, 425, 623
Lusso, E., & Risaliti, G. 2017, A&A, 602, A79
Lutz, D., Maiolino, R., Spoon, H. W. W., & Moorwood, A. F. M. 2004, A&A, 418, 465
Madau, P., & Dickinson, M. 2014, ARA&A, 52, 415
Madsen, K. K., Beardmore, A. P., Forster, K., et al. 2017, AJ, 153, 2
Magdziarz, P., & Zdziarski, A. A. 1995, MNRAS, 273, 837
Marchesi, S., Ajello, M., Marcotulli, L., et al. 2018, ApJ, 854, 49
Marchesi, S., Ajello, M., Zhao, X., et al. 2019, ApJ, 872, 8
Masoura, V. A., Mountrichas, G., Georgantopoulos, I., & Plionis, M. 2021, A&A, 646, A167
Menci, N., Fiore, F., Puccetti, S., & Cavaliere, A. 2008, ApJ, 686, 219
Merloni, A., & Heinz, S. 2008, MNRAS, 388, 1011
Middei, R., Vagnetti, F., Bianchi, S., et al. 2017, A&A, 599, A82
Mortlock, D. J., Warren, S. J., Venemans, B. P., et al. 2011, Natur, 474, 616
Murphy, K. D., & Yaqoob, T. 2009, MNRAS, 397, 1549
Noll, S., Burgarella, D., Giovannoli, E., et al. 2009, A&A, 507, 1793
Paolillo, M., Papadakis, I. E., Brandt, W. N., et al. 2023, A&A, 673, A68
Piconcelli, E., Vignali, C., Bianchi, S., et al. 2015, A&A, 574, L9
Pouliasis, E., Mountrichas, G., Georgantopoulos, I., et al. 2022, A&A, 667, A56
Pozzi, F., Vignali, C., Comastri, A., et al. 2007, A&A, 468, 603
Puccetti, S., Comastri, A., Fiore, F., et al. 2014, ApJ, 793, 26
Ricci, C., Assef, R. J., Stern, D., et al. 2017a, ApJ, 835, 105
Ricci, C., Trakhtenbrot, B., Koss, M. J., et al. 2017b, ApJS, 233, 17
Salim, S., & Narayanan, D. 2020, ARA&A, 58, 529
Salpeter, E. E. 1964, ApJ, 140, 796
Schartmann, M., Meisenheimer, K., Camenzind, M., Wolf, S., & Henning, T. 2005, A&A, 437, 861
Schreiber, C., Pannella, M., Elbaz, D., et al. 2015, A&A, 575, A74
Shirley, R., Duncan, K., Campos Varillas, M. C., et al. 2021, MNRAS, 507, 129
Snios, B., Siemiginowska, A., Sobolewska, M., et al. 2020, ApJ, 899, 127
Stalevski, M., Fritz, J., Baes, M., Nakos, T., & Popović, L. Č. 2012, MNRAS, 420, 2756
Stalevski, M., Ricci, C., Ueda, Y., et al. 2016, MNRAS, 458, 2288
Steffen, A. T., Strateva, I., Brandt, W. N., et al. 2006, AJ, 131, 2826
Stern, D. 2015, ApJ, 807, 129
Strüder, L., Briel, U., Dennerl, K., et al. 2001, A&A, 365, L18
Thorne, J. E., Robotham, A. S. G., Davies, L. J. M., et al. 2021, MNRAS, 505, 540
Torres-Albà, N., Marchesi, S., Zhao, X., et al. 2021, ApJ, 922, 252
Tsai, C.-W., Eisenhardt, P. R. M., Wu, J., et al. 2015, ApJ, 805, 90
Turner, M. J. L., Abbey, A., Arnaud, M., et al. 2001, A&A, 365, L27
Ulrich, M.-H., Maraschi, L., & Urry, C. M. 1997, ARA&A, 35, 445
Ursini, F., Bassani, L., Panessa, F., et al. 2018, MNRAS, 474, 5684
Vagnetti, F., Turriziani, S., & Trevese, D. 2011, A&A, 536, A84
Verner, D. A., Ferland, G. J., Korista, K. T., & Yakovlev, D. G. 1996, ApJ, 465, 487
Vito, F., Brandt, W. N., Lehmer, B. D., et al. 2020, A&A, 642, A149
Vito, F., Brandt, W. N., Stern, D., et al. 2018, MNRAS, 474, 4528
Wang, T., Schreiber, C., Elbaz, D., et al. 2019, Natur, 572, 211
Webb, N. A., Coriat, M., Traulsen, I., et al. 2020, A&A, 641, A136
Werner, M. W., Roellig, T. L., Low, F. J., et al. 2004, ApJS, 154, 1
Wik, D. R., Hornstrup, A., Molendi, S., et al. 2014, ApJ, 792, 48
Wu, J., Tsai, C.-W., Sayers, J., et al. 2012, ApJ, 756, 96
Yang, G., Boquien, M., Brandt, W. N., et al. 2022, ApJ, 927, 192
Yang, G., Boquien, M., Buat, V., et al. 2020, MNRAS, 491, 740
Yang, G., Brandt, W. N., Luo, B., et al. 2016, ApJ, 831, 145
Yang, G., Caputi, K. I., Papovich, C., et al. 2023, ApJL, 950, L5
Yaqoob, T. 2012, MNRAS, 423, 3360
Zappacosta, L., Comastri, A., Civano, F., et al. 2018a, ApJ, 854, 33
Zappacosta, L., Piconcelli, E., Duras, F., et al. 2018b, A&A, 618, A28
Zappacosta, L., Piconcelli, E., Giustini, M., et al. 2020, A&A, 635, L5
Zhao, X., Civano, F., Fornasini, F. M., et al. 2021a, MNRAS, 508, 5176
Zhao, X., Marchesi, S., Ajello, M., et al. 2019, ApJ, 870, 60
Zhao, X., Marchesi, S., Ajello, M., et al. 2021b, A&A, 650, A57
Zhao, X., Marchesi, S., Ajello, M., Balokovic, M., & Fischer, T. 2020, ApJ, 894, 71